



**HAL**  
open science

# The impact of typhoons on sediment connectivity: lessons learnt from contaminated coastal catchments of the Fukushima Prefecture (Japan)

Caroline Chartin, O. Evrard, J. Patrick Laceby, Yuichi Onda, Catherine Otle, Irène Lefevre, Olivier Cerdan

## ► To cite this version:

Caroline Chartin, O. Evrard, J. Patrick Laceby, Yuichi Onda, Catherine Otle, et al.. The impact of typhoons on sediment connectivity: lessons learnt from contaminated coastal catchments of the Fukushima Prefecture (Japan). *Earth Surface Processes and Landforms*, 2017, 42 (2), pp.306 - 317. 10.1002/esp.4056 . hal-01849975

**HAL Id: hal-01849975**

**<https://brgm.hal.science/hal-01849975>**

Submitted on 26 May 2020

**HAL** is a multi-disciplinary open access archive for the deposit and dissemination of scientific research documents, whether they are published or not. The documents may come from teaching and research institutions in France or abroad, or from public or private research centers.

L'archive ouverte pluridisciplinaire **HAL**, est destinée au dépôt et à la diffusion de documents scientifiques de niveau recherche, publiés ou non, émanant des établissements d'enseignement et de recherche français ou étrangers, des laboratoires publics ou privés.

1 **The impact of typhoons on sediment connectivity: Lessons learnt from**  
2 **contaminated coastal catchments of the Fukushima Prefecture (Japan)**

3 Caroline Chartin<sup>1,2\*</sup>, Olivier Evrard<sup>1,\*</sup>, J. Patrick Laceby<sup>1</sup>, Yuichi Onda<sup>3</sup>, Catherine Ottlé<sup>1</sup>,  
4 Irène Lefèvre<sup>1</sup>, Olivier Cerdan<sup>4</sup>

5

6 <sup>1</sup> *Laboratoire des Sciences du Climat et de l'Environnement (LSCE/IPSL) – Unité Mixte de Recherche*  
7 *8212 (CEA, CNRS, UVSQ), Université Paris-Saclay, 91198-Gif-sur-Yvette Cedex, France*

8 <sup>2</sup> *Georges Lemaître Centre for Earth and Climate Research, Earth and Life Institute, Université*  
9 *Catholique de Louvain, 1348 Louvain-la-Neuve, Belgium*

10 <sup>3</sup> *Center for Research in Isotopes and Environmental Dynamics (CRIED), Tsukuba University,*  
11 *Tsukuba, Japan*

12 <sup>4</sup> *BRGM, ARN, 3 av. Claude Guillemin, BP 6009, 45060 Orléans, France*

13 *\*Corresponding authors: C. Chartin ([caroline.chartin@uclouvain.be](mailto:caroline.chartin@uclouvain.be)), O. Evrard*  
14 *([olivier.evrard@lsce.ipsl.fr](mailto:olivier.evrard@lsce.ipsl.fr))*

15

16 **Keywords:** storm events; soil erosion; flooding; sediment contamination; radiocesium

17 **Abstract:** Sediment connectivity characterizes the physical transfer of sediment through different  
18 geomorphic compartments in catchments due to sediment detachment, transport and deposition.

19 Quantifying and modelling sediment connectivity is therefore a key prerequisite to improving our

20 understanding of the dispersion of particle-borne contaminants, especially in catchments exposed to

21 highly erosive climates. The objective of this study is to provide novel insights into typhoon impacts

22 on sediment connectivity from hillslopes to rivers. The dispersion of particle-bound cesium-137

23 (<sup>137</sup>Cs) was investigated in two coastal catchments draining the main contamination plume from the

24 Fukushima Daiichi Nuclear Power Plant accident. Five sampling campaigns were carried out from  
25 November 2011 to November 2015, after each typhoon season. The spatial and temporal evolution of  
26  $^{137}\text{Cs}$  contamination was investigated through the calculation of  $^{137}\text{Cs}$  enrichment ratios in sediment  
27 relative to nearby soils. Rainfall erosivity ( $\text{EI}_{30}$ ) associated with the main typhoons that occurred prior  
28 to each sampling campaign were computed, mapped, and finally used to improve a topographic-based  
29 Index of Connectivity. From 2011 to 2015, mean contamination levels in Mano and Niida catchments  
30 decreased from  $11.9 \text{ kBq kg}^{-1}$  to  $3.3 \text{ kBq kg}^{-1}$  and from  $34.1 \text{ kBq kg}^{-1}$  to  $8.0 \text{ kBq kg}^{-1}$ , respectively.  
31 Regional mean  $\text{EI}_{30}$  ranged from  $262 \text{ MJ mm ha}^{-1} \text{ h}^{-1}$  for typhoon Jelawat (2012) to  $1695 \text{ MJ mm ha}^{-1}$   
32  $\text{h}^{-1}$  for typhoon Roke (2011). Typhoons Roke (2011) and Etau (2015) showed the highest connectivity  
33 from contaminated sources to the rivers, and induced a significant export of sediment to the ocean. In  
34 2013 a slight increase in  $^{137}\text{Cs}$  levels in river sediments occurred, likely resulting from the first step in  
35 decontamination works and the occurrence of two consecutive typhoons. Importantly, this research  
36 provides new insights into the connectivity of the main sources of sediments contaminated with  
37 radiocesium in Fukushima Prefecture and their temporal evolution, which will help with ongoing  
38 decontamination efforts.

## 39 1. Introduction

40 Sediment connectivity corresponds to the physical transfer of sediment from a source to a sink through  
41 sediment detachment, transport and deposition processes (Croke et al., 2013; Fryirs, 2013). This  
42 transfer is controlled by the type of sediment movement between catchment morphological  
43 compartments (i.e. within hillslopes, between hillslopes and river channels, and within river channels)  
44 (Bracken et al., 2013). Sediment connectivity encompasses two interrelated components: structural  
45 connectivity, which describes the physical links between compartments (i.e. morphology), and  
46 functional connectivity, which relates to the processes involved in sediment movements (e.g. erosion  
47 processes, transport, and energy vectors as water or wind) (Bracken et al., 2015). Sediment  
48 connectivity is the culmination of multiple processes, from particle detachment to deposition, where  
49 different systemic compartments may potentially act as a sediment source, pathway or sink  
50 (Wainwright et al., 2001; Parsons et al., 2006). Importantly, sediment connectivity changes in space

51 and time depending on the frequency-magnitude distribution of the detachment and transport  
52 processes, the spatial and temporal feedbacks between these processes, and the dominant mechanisms  
53 of sediment detachment and transport (Bracken et al., 2015). Although recent system-based research  
54 improved our understanding of sediment sources, transfer processes and sinks in catchments (e.g.  
55 Heckmann and Schwanghart, 2013; López-Vicente et al., 2013), sediment connectivity remains  
56 difficult to quantify, model and validate.

57 The Tohoku tsunami, induced by the March 2011 earthquake, impacted the Fukushima Daiichi  
58 Nuclear Power Plant (FDNPP) resulting in the largest release of radionuclides since the Chernobyl  
59 accident (Chino et al., 2011). Approximately 20% of these radionuclides were deposited within the  
60 Fukushima Prefecture (Kawamura et al., 2011; Kobayashi et al., 2013; Groëll et al., 2014). Currently,  
61 radiocesium ( $^{134}\text{Cs}$  and  $^{137}\text{Cs}$ ) presents the most serious short and long-term health risk (Kitamura et  
62 al., 2014; Saito et al., 2015). In June 2011, soils characterized by  $^{137}\text{Cs}$  activities exceeding 100 kBq  
63  $\text{m}^2$  covered  $\sim 3000 \text{ km}^2$  in the region (MEXT, 2011). As radiocesium is strongly-bound to fine soil  
64 particles (i.e. clays and silts) (Tamura et al., 1964; Motha et al., 2002), the transfer of this contaminant  
65 from hillslopes to rivers is likely to be strongly influenced by sediment connectivity between  
66 catchment compartments.

67 The Fukushima Prefecture is characterized by high-relief topography and is subject to two main  
68 seasonal hydro-sedimentary regimes; spring snow melts and wet summers often typified by typhoon  
69 events known to produce catastrophic floods in tropical areas (Imamure and Van To, 1997; Cheng et  
70 al. 2005). The succession of these seasonal events leads to the erosion of contaminated soils and then  
71 to the export of radioactive material to the coastal plains (Chartin et al., 2013; Evrard et al. 2013). In  
72 particular, typhoon Roke (September 2011) resulted in elevated radiocesium concentrations sampled  
73 in suspended riverine material in the Fukushima Prefecture (Nago et al., 2013; Ueda et al., 2013;  
74 Mouri et al., 2014). Most of the rivers monitoring devices were damaged during the earthquake and  
75 tsunami, and river monitoring was only operational in the Abukuma River basin ( $5172 \text{ km}^2$ ) that drains  
76 moderately contaminated soils. For this basin, more than 60% of the total radiocesium flux transported  
77 between August 2011 and May 2012 occurred during typhoon Roke (Yamashiki et al., 2014).

78 Recently, several river monitoring devices were also damaged during typhoon Etou in September  
79 2015.

80 To counter the lack of river monitoring devices, alternative methods of tracking the contamination  
81 dispersion from hillslopes to rivers channels have been developed within coastal catchments draining  
82 the pollution plume. Sediment fingerprinting techniques used the spatial pattern of radioactive fallout  
83 (i.e., the variable  $^{110m}\text{Ag}$ : $^{137}\text{Cs}$  activity ratio) in soils to trace the export of riverine sediment (Chartin et  
84 al., 2013; Lepage et al., 2014a). Another technique consisted of measuring radioactive dose rates on  
85 soils and recently deposited river sediments (e.g. mud drapes on channel-bed sand) (Evrard et al.,  
86 2013; Evrard et al., 2014). This showed that the succession of the hydro-sedimentary events (i.e.  
87 typhoons and snowmelt runoff) led to the rapid decrease of radiation dose levels in river sediment in  
88 2011-2012, and an increase after the 2013 typhoons due to renewed soil erosion. These tracing  
89 approaches provide complementary methods to characterise sediment connectivity between hillslopes  
90 and rivers channels in the absence of sediment monitoring devices, but a method to quantify spatial  
91 variations of sediment connectivity in time is still lacking.

92 The development of geomorphometric indices by means of GIS-based methods provides a way to  
93 identify and delineate areas with potential erosion and deposition, and dominant pathways between  
94 catchment compartments, contributing to sediment connectivity assessment in various contexts (e.g.  
95 Lane et al., 2009; Heckmann and Schwanghart, 2013). In ungauged coastal catchments of Fukushima  
96 Prefecture, a connectivity index identified the most potential contributive source areas of contaminated  
97 sediments (i.e. croplands located in valley bottoms and coastal plains) (Chartin et al., 2013). However,  
98 this index was originally designed to assess connectivity based on landscape information only (i.e.  
99 morphology and land cover), mainly describing the structural component of sediment connectivity  
100 without an effective integration of rainfall event characteristics, a functional component of sediment  
101 connectivity (Borselli et al., 2008). The principal limitation of this approach is that it only describes an  
102 intrinsic property of the landscape that is independent of the forcing events. In areas characterized by  
103 temperate climate regimes or for long-term average connectivity assessments, this limitation is  
104 acceptable. However in the context of tropical areas where the forcing events can differ by several

105 orders of magnitude, the amplitude of the transport agent may solicit different levels of connectivity  
106 and therefore imply very different hydro-sedimentary dynamics.

107 In this context, the objective of the paper is to provide novel insights into typhoon impacts on spatial  
108 and temporal evolution of sediment connectivity in coastal catchments contaminated with radiocesium  
109 in the Fukushima Prefecture (Japan). First, the examination of five sediment sampling campaigns  
110 after each typhoon season since the FDNPP accident, from 2011 to 2015, provides a foundation for  
111 understanding sediment connectivity through the calculation of  $^{137}\text{Cs}$  enrichment ratios (ER). Second,  
112 spatial variability of typhoon rainfall erosivity is studied for the most intensive typhoons that occurred  
113 prior to each sampling campaign. Finally, a topography-based index of connectivity is refined by  
114 integrating typhoon event rainfall erosivity as functional connectivity parameter, and comparing it to  
115 the  $^{137}\text{Cs}$  ER. This research provides more understanding on the impact of typhoons on radiocesium  
116 transfer necessary for improving the management of post-accident radiocesium fallout in the  
117 Fukushima region.

## 118 2. Materials and methods

### 119 2.1. Study area

120 Most of the terrestrial fallout from the FDNPP accident occurred over the eastern part of the  
121 Fukushima Prefecture (Fig. 1). Soil contamination  $> 10 \text{ kBq kg}^{-1}$  of  $^{137}\text{Cs}$  occurred mostly within small  
122 catchments ( $< 700 \text{ km}^2$ ) draining to the Pacific Ocean, with the highest contamination levels in the  
123 coastal mountain range located northwest of the FDNPP. These coastal catchments are typical for  
124 Japan, dominated by steep forested hillslopes in upstream mountainous areas (up to 1000 m elevation),  
125 and by paddy fields and built-up areas in valley bottoms and coastal plains. River profiles are short,  
126 steep and strongly incised due to the geomorphological and hydrological contexts with the Japan  
127 archipelago being long and narrow, geologically young, tectonically active, and subject to a wet  
128 climate. Japanese catchments are frequently subject to heavy rainfall events (i.e. tropical storms and  
129 typhoons) (Lacey et al., 2016) likely leading to short-duration floods with high concentrations in

130 contaminated sediments (Yamaguchi et al., 2014; Evrard et al., 2015). Moreover, the ratio of bedload  
131 to total load transported by Japanese rivers can reach 0.6 to 0.8 (e.g. Ohmori, 1991; Oguchi, 1997).

132 The climate in the study area is characterized by a hot and humid summer with monsoonal activity in  
133 June-July and convective storms and an active typhoon season occurring mainly from July to October.  
134 The region receives  $\sim 1420 \text{ mm yr}^{-1}$  of precipitation and rainfall erosivity is  $3696 \text{ MJ mm ha}^{-1} \text{ h}^{-1} \text{ yr}^{-1}$   
135 (Lacey et al., 2016) with the majority of precipitation (60%) and rainfall erosivity (86%) occurring  
136 between June and October (Fig. 2). Typhoons are responsible for 22% of the annual precipitation ( $422$   
137  $\text{mm yr}^{-1}$ ) and 40% of the annual rainfall erosivity ( $1462 \text{ MJ mm ha}^{-1} \text{ h}^{-1} \text{ yr}^{-1}$ ) (Lacey et al., 2016). The  
138 typhoons that occurred in the study area right prior each sampling campaign related to this study are  
139 identified in Figure 2: typhoon Roke (2011), typhoon Jelawad (2012), typhoons Wipha and Francisco  
140 (2013), typhoons Phanfone and Vongfong (2014), and typhoon Etau (2015).

141 Based on the geomorphological and climatic contexts of the eastern region of the Fukushima  
142 Prefecture, two representative coastal catchments were investigated, (i.e. the Mano and Niida  
143 catchments), covering  $\sim 450 \text{ km}^2$  North West of the FDNPP (Fig. 1). These steep short rivers originate  
144 in the coastal mountain range, from an upstream altitude of 700 to 900 m a.s.l and drain into the  
145 Pacific Ocean (Fig. 3a). The upstream sections of the Mano and Niida catchments are the most  
146 contaminated with  $^{137}\text{Cs}$ , with contamination decreasing downstream towards the coastal plain (Fig. 1)  
147 (Chartin et al., 2013). The three main land uses, forests (deciduous and evergreen), croplands  
148 (predominantly rice paddies) and built-up areas, cover 73%, 12% and 15% of the study area  
149 respectively (Fig. 3b).

## 150 2.2. Enrichment ratios (ER) in $^{137}\text{Cs}$ of river drape sediments

151 Lag deposit sediment samples (i.e. mud drapes deposited on channel-bed sand) were collected along  
152 the main rivers draining the Mano and Niida catchments and some of their major tributaries after each  
153 typhoon season between 2011 and 2015. At each sampling site, five to ten surface scrapes of deposited  
154 sediment, collected along a 5 m river reach with a plastic spatula, were composited into one sample.  
155 Upon returning to the laboratory, the samples were oven-dried ( $60 \text{ }^\circ\text{C}$ ) for 48 h and then dry-sieved

156 (<2 mm). These samples were then ground to a fine powder, weighed, packed into 15 ml pre-tared  
157 polyethylene containers and sealed airtight prior to analyses.

158 <sup>137</sup>Cs activities were determined by gamma spectrometry using low-background coaxial N- and P-  
159 types HPGe detectors. Counting time of soil and sediment samples varied between 3×10<sup>4</sup> and 8×10<sup>4</sup> s.  
160 The <sup>137</sup>Cs activities were measured at the 661 keV emission peak; errors reached ca. 5% at the 95%  
161 confidence level. All measured counts were corrected for background levels measured at least every 2  
162 months as well as for detector and geometry efficiencies. Results were systematically expressed in Bq  
163 kg<sup>-1</sup> of dry weight. Counting efficiencies and quality assurance were conducted using certified  
164 International Atomic Energy Agency (IAEA) reference materials prepared in the same containers as  
165 the samples. All radionuclide activities were decay-corrected to March 15, 2011.

166 The <sup>137</sup>Cs ER provides a quick and robust indication of the magnitude of <sup>137</sup>Cs contamination of the  
167 sediments compared with the local background contamination of soils. Hence sediments either have  
168 enriched (ER > 1) or depleted (ER < 1) <sup>137</sup>Cs activities relative to their most proximal sources  
169 depending on source and sink dynamics for nearby soil sources areas. ER values were calculated with  
170 all activities decay-corrected to March 15, 2011, as follows (Eq .1):

$$171 \quad ER = \frac{{}^{137}\text{Cs activity } \left(\frac{\text{Bq}}{\text{kg}}\right) \text{ in the sediment sample}}{{}^{137}\text{Cs background activity (Bq/kg) in nearby soil sources}} \quad (1)$$

172 The <sup>137</sup>Cs background activity in soils was determined for the whole study area through a mapping  
173 procedure based on a set of 2200 observations sampled in June and July 2011 and provided by the  
174 Japanese Ministry of Education, Culture, Sports, Science and Technology (MEXT). Detailed  
175 information about the Cs background mapping procedure is reported in Chartin et al. (2013). The <sup>137</sup>Cs  
176 background activity used in the ER calculation (eq. 1) was the mean value predicted for pixels located  
177 under cropland in the 100 m<sup>2</sup> area surrounding each of the river sampling sites.

### 178 2.3. Principles of the connectivity index

179 The connectivity index (IC) developed by Borselli et al., (2008) originally depicts the general  
180 structural connectivity that potentially occurs between different parts of a catchment (i.e. sources and

181 sinks). The basic form of the connectivity index is a ratio between an upslope component ( $D_{up}$ ) and a  
182 downslope component ( $D_{dn}$ ; Borselli et al., 2008):

$$183 \quad IC = \log_{10}\left(\frac{D_{up}}{D_{dn}}\right) \quad (2)$$

184 The IC value is defined in the range of  $-\infty$  ;  $+\infty$ , with the higher the IC values indicating a lower  
185 potential for sediment produced upslope to be deposited in nearest downstream sinks. The upslope  
186 component ( $D_{up}$ ) corresponds to the potential that sediment produced in the upslope contributing area  
187 be routed to the considered downstream pixel area.  $D_{up}$  is estimated as follows:

$$188 \quad D_{up} = \sqrt{A} \bar{S} \bar{W} \quad (3)$$

189 Where  $A$  is the upslope contributing area ( $m^2$ ),  $\bar{S}$  is the average slope gradient ( $m/m$ ) of the upslope  
190 contributing area, and  $\bar{W}$  is the average weighting factor of the upslope contributing area (see § 2.5).

191 The downslope component ( $D_{dn}$ ) characterizes the potential that the sediment, which is routed through  
192 the considered pixel area, has to be then transported downstream to the nearest sink along the flow  
193 path.  $D_{dn}$  is estimated as follows:

$$194 \quad D_{dn} = \sum_i \frac{d_i}{S_i W_i} \quad (4)$$

195 Where  $d_i$  is the length of the flow path along the  $i^{th}$  cell according to the steepest slope ( $m$ ),  $S_i$  and  $W_i$   
196 are the slope gradient and the weighting factor of the  $i^{th}$  cell respectively.

#### 197 2.4. Refinement to the index of sediment connectivity

198 Three changes were made to the model depicted above: i) thresholds were applied to the slope factor  
199 to adapt the model to the context of mountainous catchments (Cavalli et al., 2012), ii) the C-factor, as  
200 defined in the USLE equation (Wischmeier and Smith, 1978; Renard et al., 1997) and introduced in  
201 the calculation of the first version of the index (Borselli et al., 2008), was used as a weighting factor  
202 but was adapted from one typhoon event to another accordingly to the observed evolution of  
203 vegetation cover, and iii) a rainfall erosivity weighting ( $R_t$ ) factor was added as a second weighting  
204 factor to account for the specificity of typhoon events (i.e., event frequency, intensity and rainfall

205 amount). In this work, we focused on the main typhoons that occurred prior to each sampling  
206 campaign (i.e., Roke in 2011, Jelawad in 2012, Wipha and Francisco in 2013, Phanfone and Vongfong  
207 in 2014 and Etau in 2015) (Fig. 2). Two events were chosen for years 2013 and 2014 as these events  
208 occurred very close in time. So, the revised version of the IC model ( $IC_{rev}$ ) used here corresponds to  
209 the following ratio:

$$210 \quad IC_{rev} = \log_{10} \left( \frac{\sqrt{A} \bar{S} \bar{C} \bar{R}_t}{\sum_i S_i C_i R_{t_i}} \right) \quad (5)$$

### 211 *Slope factor*

212 Morphometric parameters (A, S) were derived from a Digital Elevation Model (DEM) with a 10 m  
213 resolution provided by the Geospatial Information Authority of Japan (GSI) from the Ministry of  
214 Land, Infrastructure, Transport and Tourism (<http://www.gsi.go.jp/>; Fig. 1). This DEM was derived  
215 from LIDAR airborne monitoring surveys. A minimum threshold value of 0.005 m/m was applied to  
216 the slope layer to avoid infinite values in Eq. 4 (Borselli et al., 2008), and a maximum threshold value  
217 of 1 m/m was applied to avoid a bias (very high IC values) on the steepest slopes (Cavalli et al., 2012).

### 218 *Cover factor*

219 The Cover factor (C-factor) accounts for the effects of plants, soil cover, soil biomass, and soil  
220 disturbing activities on soil erosion (i.e. particle detachment)(Wischmeier and Smith, 1978; Renard et  
221 al., 1991; Renard et al., 2007). It also accounts for the effects of vegetation on water infiltration.  
222 Values were determined based on terrain observations made during each fieldwork campaign and data  
223 found in the literature (Kitahara et al., 2000; Shiono et al., 2002; Yoshikawa et al., 2004). A C-factor  
224 value of 0.01 was applied to forested areas, and 1 to bare soils and built-up areas for the experiment  
225 period. Values for cropland areas were 0.38 for 2011, 0.17 for 2012 and 0.04 for the remaining years.  
226 These values were applied to land use classes determined by a multitemporal and multispectral  
227 classification of images from SPOT-4 and SPOT-5 satellites (Chartin et al., 2013).

### 228 *Rainfall erosivity factor*

229 To calculate rainfall erosivity, precipitation data recorded in 10 minute intervals between 2011 and  
 230 2015 was downloaded from 40 monitoring stations located within 100 km of the FDNPP that are  
 231 operated by Japan Meteorological Agency's Automated Meteorological Data Acquisition System  
 232 (AMeDAS). The Rainfall Intensity Summarisation Tool (RIST) software (USDA, 2013) was used to  
 233 determine the rainfall erosivity ( $EI_{30}$ ) of each typhoon (Lacey et al., 2016). Rainfall erosivity is a  
 234 product of the energy (E) of the rainfall event and its maximum 30-minute intensity ( $I_{30}$ ) (Renard and  
 235 Freimund, 1994). RIST was used to calculate the rainfall erosivity for 3 days before and 3 days after  
 236 each typhoon event to ensure that all the potential rainfall erosivity associated with the event was  
 237 included.

238 The criteria used to identify the erosive events were: 1) cumulative rainfall of an event was  $>12.7\text{mm}$ ;  
 239 and 2) rainfall accumulations  $<1.27\text{mm}$  for a 6 hour period separated events into two different periods.  
 240 These criteria isolated the period of the typhoon events for which  $EI_{30}$  were calculated via:

$$EI_{30} = \left( \sum_{r=1}^o e_r v_r \right) I_{30} \quad (6)$$

241 with  $e_r$  representing rainfall energy per unit depth of rainfall in  $\text{MJ ha}^{-1} \text{mm}^{-1}$ ,  $v_r$  is the volume of  
 242 rainfall (mm) during a given time period (r), and  $I_{30}$  is the maximum rainfall intensity over a 30 minute  
 243 period of the rainfall event ( $\text{mm h}^{-1}$ ). For each time interval,  $e_r$  is calculated as:

$$e_r = 0.29[1 - 0.72^{(-0.05i_r)}] \quad (7)$$

244 with  $i_r$  being the rainfall intensity for the time interval ( $\text{mm h}^{-1}$ ) (Brown and Foster, 1987).

245 The  $EI_{30}$  was then mapped based on the values computed for all the stations located within the 100 km  
 246 area around the FDNPP (see § 2.6). Then, we computed the rainfall weighing ( $R_t$ ) factor as follows:

$$R_t = \frac{EI_{30}}{EI_{30max}} \quad (8)$$

248 Where  $EI_{30max}$  is the maximum  $EI_{30}$  value predicted amongst the five considered typhoon events within  
249 the restricted area of the study catchments. This normalization of the  $R_t$  factor allows to avoid bias  
250 induced by high  $EI_{30}$  values, and to provide same range values as for S and C factors.

## 251 2.5. Mapping the rainfall erosivity factor

252 The  $EI_{30}$  values were used to compute maps of typhoon erosivity at a resolution of 250 m over the  
253 eastern part of the Fukushima Prefecture. A regression approach, based on relationships established  
254 between the  $EI_{30}$  data and spatially distributed covariates, was used to produce these maps. The  
255 covariates used in the modelling procedure were morphometric attributes (elevation, slope and  
256 aspect), climatic data (monthly mean rainfall and mean temperature), distance to the coast and  
257 geographical coordinates. Detailed information about the source data and the computation of the  
258 covariates layers is provided in Laceby et al. (2016).

259 The spatially continuous covariates were rescaled at a 250 m resolution in ArcGIS10 (ESRI, 2011)  
260 with bilinear interpolation. The spatial distribution of typhoon rainfall erosivity in the eastern part of  
261 the Fukushima prefecture was then modelled with Generalized Additive Models (GAM; Hastie and  
262 Tibshirani, 1986). GAMs were fitted on five datasets, i.e.,  $EI_{30}$  values computed for typhoon Roke  
263 (2011), typhoon Jelawad (2012), typhoon Etou (2015), and sums of  $EI_{30}$  values computed for typhoons  
264 Wipha and Francisco (2013), and for typhoons Phanfone and Vongfong (2014). The GAM technique  
265 is a generalization of linear regression models in which the coefficients can be a set of smoothing  
266 functions, accounting then for the non-linearity that could exist between the dependent variable and  
267 covariates. GAM specifies a distribution for the conditional mean  $\mu(Y)$  and a link function  $g$  relating  
268 this latter to an additive function of the covariates:

$$269 \quad g[\mu(Y)] = \alpha + f_1X_1 + f_2X_2 + \dots + f_pX_p \quad (9)$$

270 where Y is the dependent variable,  $X_1, X_2, \dots, X_p$  represent the covariates and the  $f_i$ 's the smooth (non-  
271 parametric) functions.

272 Based on  $EI_{30}$  data computed for the 40 rain stations, GAMs were fitted to spatially model the rainfall  
273 erosivity of the selected typhoons over the eastern part of Fukushima prefecture including the two  
274 investigated catchments (Fig. 1). A Gaussian distribution model incorporated the conditional mean  
275  $\mu(Y)$  and a log-linear link function  $g(\mu) = \log(\mu)$  was implemented due to the predominant logarithmic  
276 distribution of the data. The GAM models were built using regression splines, and the smoothing  
277 parameters were estimated by penalized Maximum Likelihood to avoid an over-fitting (Wood, 2001).  
278 A leave-one-out cross-validation procedure was applied to each fitted models, and then mean error  
279 (ME) and root mean square error (RMSE) were calculated to quantify their goodness of fit.

280

### 281 3. Results and discussion

#### 282 3.1. Evolution of radioactive contamination in river drape sediments

283 Evolutions of  $^{137}\text{Cs}$  contents and  $^{137}\text{Cs}$  ER of river sediment deposits were examined to investigate the  
284 evolution of sediment connectivity between contaminated hillslopes and river channels (Figs. 4 and 5).  
285 Mean contamination levels of the sediments in the Niida river were 2 to 3 times higher than in the  
286 Mano river (Fig. 4). This reflects the differences observed between the contamination background of  
287 soil sources within the two catchments (Fig. 1). Mean sediment contamination decreased substantially  
288 from 2011 to 2012 and from 2014 to 2015, with a more slight decrease from 2012 to 2013 (Fig. 4).  
289 From 2011 to 2015, mean contamination levels in Mano catchment and Niida catchment decreased  
290 from  $11.9 \text{ kBq kg}^{-1}$  (SD 6.8;  $n=5$ ) to  $3.3 \text{ kBq kg}^{-1}$  (SD 2.0;  $n=18$ ) and from  $34.1 \text{ kBq kg}^{-1}$  (SD 29.0;  
291  $n=16$ ) to  $8.0 \text{ kBq kg}^{-1}$  (SD 5.5;  $n=19$ ), respectively. The only exception is a slight increase of mean  
292 sediment contamination observed from 2012 to 2013 in the Niida River (from  $17.7 \text{ kBq kg}^{-1}$  (SD 14.5;  
293  $n=18$ ) to  $20.4 \text{ kBq kg}^{-1}$  (SD 15.3;  $n=22$ )).

294 Following the first typhoon season occurring after the FDNPP accident, ER values were  
295 predominantly greater than 1.5 in both catchments (red dots in Fig. 5) confirming dynamic sediment  
296 regimes that connected hillslopes to rivers, and that a massive export of contaminated particles  
297 occurred. This observation can locally be reversed in the upstream part of catchments (river sediments

298 had lower  $^{137}\text{Cs}$  activities than nearby soils), especially where valley bottoms are narrow and  
299 uncultivated and, consequently, scarce sediment source areas (Fig. 3).

300 From 2011 to 2012, ER values of most samples from mountainous upstream areas (brown to white  
301 areas in Figure 5) decreased (median value of ER evolved from 1.8 to 0.7 from 2011 to 2012). A slight  
302 increase of ER values occurred in 2013 (median ER = 0.8) just after two consecutive typhoons (Wipha  
303 and Francisco) for most of the samples analysed in both catchments, confirming the observations that  
304 hillslope soil erosion processes were renewed (Evrard et al., 2014). From 2013 to 2015, ER values of  
305 most samples from both catchments decreased (median ER = 0.4 for year 2015). A new element to  
306 take into account for this period is the very rapid progress of the decontamination works that have  
307 remobilized contaminated material by erosion processes that were formerly protected by the post-  
308 accident vegetation regrowth, and then rapidly removed the contamination from the surface of the  
309 areas covered by non-permanent vegetation.

### 310 3.2. Typhoon characteristics and mapping

311 Erosivity of the most intense typhoons that occurred prior to each sampling campaign was computed  
312 for the meteorological stations located within the 100 km area around FDNPP (Table 1). Mean  $\text{EI}_{30}$   
313 values ranged from 262 MJ mm ha<sup>-1</sup> h<sup>-1</sup> (SD 197; n=36) for typhoon Jelawat in 2012 to 1695 MJ mm  
314 ha<sup>-1</sup> h<sup>-1</sup> (SD 1066; n=39) for typhoon Roke in 2011. GAMs were fitted to the observed values.  
315 Validation procedure of the models resulted in  $R^2$  varying between 0.83 and 0.95, and predicted values  
316 showed similar distributions to those of observed values (Table 1).

317 The rainfall erosivity maps ( $\text{EI}_{30}$  in MJ mm ha<sup>-1</sup> h<sup>-1</sup>) are depicted at two different scales, the 100 km  
318 buffer area around FDNPP and the two investigated catchments in Figure 6A and Figure 6B,  
319 respectively. At the regional scale, all the typhoons except Jelawat (2011) showed the same general  
320 spatial pattern with typhoon erosivity strongly decreasing from the coast (east) to the inland areas  
321 (west) (Fig. 6A). This reflects the role of the Pacific Ocean on driving tropical storms and typhoons.  
322 Accordingly, the coastal plain and coastal mountainous ranges, including the FDNPP and a large part  
323 of the contamination plume with high levels of  $^{137}\text{Cs}$  contamination, were submitted to greater typhoon

324 erosivity than the less contaminated Abukuma River valley. This spatial pattern was also observed at  
325 the regional scale for monthly mean rainfall erosivity during wet and typhoon season (from June to  
326 October), i.e. during the most erosive annual period (Lacey et al., 2016).

327 At the scale of the two investigated catchments, rainfall erosivity decreased from the coastal plains to  
328 the upslope mountainous areas for the typhoon Roke (2011), typhoons Wipha and Francisco (2013)  
329 and typhoons Phanfone and Vongfong (2014) (Fig. 6B). Typhoons Jelawat (2012) and Etau (2015),  
330 the least and the most erosive events respectively, had a positive gradient of rainfall erosivity from the  
331 coast to the mountain range. According to the typhoon erosivity maps, the Mano and Niida catchments  
332 were submitted to rather similar rainfall erosivity for each individual event, e.g. mean  $EI_{30}$  was 653 MJ  
333  $\text{mm ha}^{-1} \text{h}^{-1}$  (SD 146) and 608 MJ  $\text{mm ha}^{-1} \text{h}^{-1}$  (SD 209) for Mano and Niida catchments respectively  
334 during the Wipha/Francisco event of 2013.

335 The relative intensity of the different typhoon events at the catchment scale appeared quite different  
336 from the one observed at the regional scale. According to the observed and predicted  $EI_{30}$  values  
337 (Table 1), typhoon Roke (2011) and typhoon Etau (2015) had similar mean erosivities at the regional  
338 scale, i.e. mean observed values of 1695 MJ  $\text{mm ha}^{-1} \text{h}^{-1}$  and 1581 MJ  $\text{mm ha}^{-1} \text{h}^{-1}$  respectively.  
339 However, the SD was higher for typhoon Etau (SD 1577) than for typhoon Roke (SD 1066) indicating,  
340 in these cases of right skewed distributions, that the erosivity magnitude of typhoon Etau had locally  
341 reached higher values than maximum values observed for typhoon Roke. Indeed, mean predicted  
342 values for typhoon Etau (2015) were two times higher than those for typhoon Roke (2011) at the scale  
343 of the two studied catchments. For example, we predicted mean  $EI_{30}$  values of 4299 MJ  $\text{mm ha}^{-1} \text{h}^{-1}$   
344 (SD 1702) for Typhoon Etau and 2099 MJ  $\text{mm ha}^{-1} \text{h}^{-1}$  (SD 520) for Typhoon Roke (Table 2). This  
345 could possibly be explained by the characteristics of these different events (e.g. path, speed, intensity).

### 346 3.3. Revised Index of Connectivity ( $IC_{\text{rev}}$ ) and relationship with $^{137}\text{Cs}$ 347 Enrichment Ratios (ER)

348 The  $EI_{30}$  maps were used to compute the revised Index of Connectivity ( $IC_{\text{rev}}$ ) for the five typhoon  
349 events (Fig. 7). The  $IC_{\text{rev}}$  maps corresponding to the different typhoon events all identify croplands and

350 built up areas as the most potentially connected sediment source areas to the river network. However,  
351 the calculated connectivity indices display very different values depending on the evolution of the  
352 vegetation cover (C-factor), but most importantly, on the differences in rainfall erosivity between  
353 events (Table 3). Although both events were characterized by equivalent C-factors,  $IC_{rev}$  values were  
354 higher for the more intense typhoon Etau (mean of -7.2; SD 1.5 in Mano catchment) than for the less  
355 intense typhoon Wipha and Francisco (mean of -8.7; SD 1.4 in Mano catchment) (Table 2, Fig. 7). In  
356 addition, maps of the  $IC_{rev}$  show variations in sediment connectivity reflecting the spatial  
357 characteristics of the event erosivity as depicted in Figure 6B. For example, the connectivity index  
358 associated with typhoon Etau (2015) increased from coastal plain to upstream mountainous areas  
359 while, on the contrary, connectivity index computed for typhoons Phanfone and Vongfong (2014)  
360 decreased in this same direction.

361 We compared the index values computed for the five typhoons events to ER values (Fig. 8). For all the  
362 events, except typhoons Phanfone and Vongfong in 2014 in the Niida catchment, a negative  
363 exponential relation was observed between  $IC_{rev}$  and ER values. Accordingly, these results clearly  
364 indicate that the higher the connectivity, the lower the potential for contaminated sediment, from  
365 nearby source areas, to be deposited at locations sampled downstream (Borselli et al., 2008).

366 Coefficients of correlations between  $IC_{rev}$  and ER values ranged between 0.01 in Mano catchment for  
367 typhoons Phanfone and Wongfong (2014) to 0.44 in Niida catchment for typhoon Etau (2015; Fig. 8).  
368 A coefficient of correlation of 0.01 was also observed in Mano catchment for typhoon Roke (2011)  
369 but cannot be considered as representative considering the low number of observed sites ( $n=5$ ). The  
370 strongest relationships between  $IC_{rev}$  and ER values were observed for the two most erosive typhoons  
371 (Roke and Etau) with the Mano and Niida catchments having a  $R^2$  of 0.29 and 0.44 respectively for  
372 typhoon Etau in 2015. Typhoon Roke was the first major typhoon after the FDNPP accident leading to  
373 the widespread erosion of initially contaminated soil sources and their export to the Pacific Ocean  
374 (Fig. 4; Yamashiki et al., 2014). Etau was the most intense typhoon that occurred at the Mano and  
375 Niida catchments scale since the accident likely leading to the flush of recently eroded material and  
376 also temporary stored contaminated material within the channels to the Pacific Ocean (Fig. 4). The

377 Mano catchment showed mainly lower coefficients of correlation than Niida catchment except for the  
378 typhoon Wipha and Francisco in 2014. The Mano catchment was originally less contaminated and had  
379 much more narrow upstream valley bottoms and also less cultivated areas than in Niida catchment (i.e.  
380 less potential connected source areas) (Fig. 1; Fig. 3). This may explain why the relationships  
381 observed between  $IC_{rev}$  and ER values for Mano catchment were lower than in the Niida catchment.

382 The results are contrasted, particularly for the less intense rainfall events. Even though, it is now well  
383 accepted that rainfall erosivity has a strong influence on sediment connectivity, sediment detachment,  
384 transport and deposition processes are complex and subject to multiple forcing that interact non-  
385 linearly in time and space. In our context, among other factors, we can cite the spatial heterogeneity of  
386 the background contamination (including the progressive decontamination works), the multiplicity of  
387 erosion processes that can either affect contaminated surface materials (e.g. surface hillslope erosion)  
388 or non-contaminated materials (mass movement, bank erosion), or the complex succession of events  
389 of different magnitude that imply progressive deposition and re-entrainment processes. This  
390 complexity explains that the relationship between connectivity and rainfall erosivity can only be  
391 qualified for the more intense typhoons that occurred in the area: Roke and Etau, but which also  
392 demonstrates the importance to incorporate the characteristics of the forcing agents when modelling  
393 water and sediment connectivity.

394 Future research should strive to improve ER and  $IC_{rev}$  modelling approaches and examine the impact  
395 and limitations of these potential factors that may be influencing the relationship between ER values  
396 and connectivity. Importantly, this research represents a significant first step towards incorporating the  
397 erosivity of rainfall directly into sediment connectivity indices, which is important in regions similar  
398 to Fukushima, where nearly half of the rainfall erosivity is derived from major rainfall events.

#### 399 4. Conclusion

400

401 Typhoons are major drivers for soil erosion, and also for potential dispersion and downstream transfer  
402 of particles bound contaminants. Here, the downstream dispersion of sediments contaminated with

403 radiocesium was investigated after five consecutive typhoon seasons (from 2011 to 2015) in two  
404 ungauged catchments draining the main contamination plume of Fukushima Prefecture.

405 From 2011 to 2015, mean contamination levels in Mano and Niida catchments decreased from 11.9  
406 kBq kg<sup>-1</sup> to 3.3 kBq kg<sup>-1</sup> and from 34.1 kBq kg<sup>-1</sup> to 8.0 kBq kg<sup>-1</sup>, respectively. Mean sediment  
407 contamination strongly decreased early after the accident, from 2011 to 2012, and then, to a lesser  
408 extent, between 2014–2015. In particular, it was demonstrated that the catchment systems and their  
409 contaminated sediment connectivity had higher correlations for events with the highest rainfall  
410 erosivity. Indeed, the highest correlations between the revised Index of Connectivity (ICrev) and the  
411 sediment ER in <sup>137</sup>Cs were observed for the most erosive typhoons, i.e. Roke in 2011 and Etau in  
412 2015. These two typhoons resulted in a high level of connectivity between sources of eroded  
413 contaminated particles and the river systems, and contributed greatly to the export of contaminated  
414 material to the Pacific Ocean. In 2013, a slight increase in <sup>137</sup>Cs levels in river sediments was  
415 observed, likely resulting from the beginning of the decontamination works and the occurrence of two  
416 consecutive typhoons (Wipha and Francisco). From 2013 to 2015, the typhoon events resulted in the  
417 dilution of the <sup>137</sup>Cs signal in river sediments by inputs of different non-contaminated subsoil sources  
418 and decontaminated surface sources relative to contaminated surface source contributions.

419 Although it remains difficult to fully validate sediment connectivity models with complex metrics of  
420 radiocesium downstream migration (ER values), this interpretation, based on both ICrev and ER  
421 values, demonstrates the importance of including individual storm erosivity and detailed vegetation  
422 cover information when quantifying sediment connectivity indices. These results indicate that the  
423 calculation of ICrev may provide a very useful tool to improve the estimation of particle-borne  
424 contaminant fluxes during extreme events, particularly in ungauged catchments.

425

426

427

428

429 **Acknowledgements:**

430 This work has been supported by the French National Research Agency (ANR) in the framework of  
431 AMORAD project (ANR-11-RSNR-0002). Assistance of Jeremy Patin, Philippe Bonté, Hugo Lepage  
432 and Hugo Jaegler for fieldwork was greatly appreciated.

433 REFERENCES:

- 434 Borselli L, Cassi P, Torri D. 2008. Prolegomena to sediment and flow connectivity in the landscape: a  
435 GIS and field numerical assessment. *Catena* **75** : 268–277.
- 436 Bracken LJ, Turnbull L, Wainwright J, Bogaart P. 2015. Sediment connectivity: a framework for  
437 understanding sediment transfer at multiple scales. *Earth Surface Processes and Landforms* **40**: 177-  
438 188.
- 439 Bracken LJ, Wainwright J, Ali GA, Tetzlaff D, Smith MW, Reaney SM, Roy AG. 2013. Concepts of  
440 hydrological connectivity: research approaches, pathways and future agendas. *Earth Science Reviews*  
441 **119**: 17–34.
- 442 Cavalli M, Trevisani S, Comiti F, Marchi L, 2012. Geomorphic assessment of spatial sediment  
443 connectivity in small Alpine catchments. *Geomorphology* **188**: 31-41.
- 444 Chartin C, Evrard O, Onda Y, Patin J, Lefèvre I, Otlé C, Ayrault S, Lepage H, Bonté Ph. 2013.  
445 Tracking the early dispersion of contaminated sediment along rivers draining the Fukushima  
446 radioactive pollution plume. *Anthropocene* **1**, 23–34.
- 447 Cheng JD, Huang YC, Wu HL, Yeh, JL, Chang CH. 2005. Hydrometeorological and landuse  
448 attributes of debris flows and debris floods during typhoon Toraji, July 29-30 2001 in central Taiwan.  
449 *Journal of Hydrology* **306(1-4)**: 161-173.
- 450 Chino M, Nakayama H, Nagai H, Terada H, Katata G, and Yamazawa H. 2011. Preliminary  
451 estimation of release amounts of <sup>131</sup>I and <sup>137</sup>Cs accidentally discharged from the Fukushima Daiichi  
452 nuclear power plant into the atmosphere. *Journal of nuclear science and technology* **48(7)**: 1129-1134.
- 453 Croke J, Fryirs K, Thompson C. 2013. Channel–floodplain connectivity during an extreme flood  
454 event: implications for sediment erosion, deposition, and delivery. *Earth Surface Processes and*  
455 *Landforms* **38(12)**: 1444–1456.
- 456 ESRI. 2011. ArcGIS Desktop: Release 10. Redlands. Environmental Systems Research Institute, CA.

457 Evrard O, Chartin C, Onda Y, Patin J, Lepage H, Lefèvre I, Ayrault S, Ottlé C, Bonté Ph. 2013.  
458 Evolution of radioactive dose rates in fresh sediment deposits along coastal rivers draining Fukushima  
459 contamination plume. *Scientific Reports* **3**, 3079.

460 Evrard O, Chartin C, Onda Y, Lepage H, Cerdan O, Lefèvre I, Ayrault S. 2014. Renewed soil erosion  
461 and remobilisation of radioactive sediment in Fukushima coastal rivers after the 2013 typhoons.  
462 *Scientific Reports* **4**, 4574.

463 Evrard O., Lacey J. P., Lepage H., Onda Y., Cerdan O., Ayrault S. 2015. Radiocesium transfer from  
464 hillslopes to the Pacific Ocean after the Fukushima Nuclear Power Plant accident: A review. *Journal*  
465 *of Environmental Radioactivity* **148**: 92–110.

466 Fryirs K. 2013. Connectivity in catchment sediment cascades: a fresh look at the sediment delivery  
467 problem. *Earth Surface Processes and Landforms* **38(1)**: 30–46.

468 Fukushima River Basin Comprehensive Information System.  
469 2013.<http://kaseninf.pref.fukushima.jp/gis/>

470 Groëll J, Quélo D, Mathieu A. 2014. Sensitivity analysis of the modelled deposition of <sup>137</sup>Cs on the  
471 Japanese land following the Fukushima accident. *International Journal of Environment and Pollution*  
472 **55(1)**: 67-75.

473 Hastie T, and Tibshirani R. 1986. Generalized additive models. *Statistical science* **1(3)**: 297-310.

474 Heckmann T and Schwanghart W. 2013. Geomorphic coupling and sediment connectivity in an alpine  
475 catchment exploring sediment cascades using graph theory. *Geomorphology* **182**: 89-103.

476 Hijmans RJ, Cameron SE, Parra JL, Jones PG, Jarvis A. 2005. Very high resolution interpolated  
477 climate surfaces for global land areas. *International Journal of Climatology* **25(15)**: 1965-1978. DOI:  
478 10.1002/joc.1276

479 Imamura F, Van To D. 1997. Flood and typhoon disasters in Viet Nam in the half century since 1950.  
480 *Natural Hazards* **15**: 71-87. Kawamura H, Kobayashi T, Furuno A, In T, Ishikawa Y, Nakayama T,

481 Shima S, Awaji T. 2011. Preliminary numerical experiments on oceanic dispersion of  $^{131}\text{I}$  and  $^{137}\text{Cs}$   
482 discharged into the ocean because of the Fukushima Daiichi nuclear power plant disaster. *Journal of*  
483 *nuclear science and technology* **48(11)**: 1349-1356.

484 Kitahara H, Okura Y, Sammori T, Kawanami A. 2000. Application of the Universal Soil Loss  
485 Equation in mountainous forests in Japan. *Journal of Forest Research* **5**: 231-236.

486 Kitamura A, Yamaguchi M, Kurikami H, Yui M, Onishi Y. 2014. Predicting sediment and cesium-137  
487 discharge from catchments in eastern Fukushima. *Anthropocene* **5**: 22-31.

488 Kobayashi T, Nagai H, Chino M, Kawamura H. 2013. Source term estimation of atmospheric release  
489 due to the Fukushima Dai-ichi Nuclear Power Plant accident by atmospheric and oceanic dispersion  
490 simulations: Fukushima NPP Accident Related. *Journal of Nuclear Science and Technology* **50(3)**:  
491 255-264.

492 Kusakabe, M., Oikawa, S., Takata, H., and Misonoo, J. 2013 Spatiotemporal distributions of  
493 Fukushima-derived radionuclides in nearby marine surface sediments. *Biogeosciences* **10**: 5019–5030.

494 Laceby JP, Chartin C, Evrard O, Onda Y, Garcia-Sanchez L, Cerdan O. 2016. Rainfall erosivity in  
495 catchments contaminated with fallout from Fukushima Daiichi nuclear power plant accident.  
496 *Hydrology and Earth System Sciences* **20**: 1-16.

497 Laceby JP, Huon S, Onda Y, Vaury V, Evrard O. (in review) Tracing particulate matter sources in  
498 coastal catchments of the Fukushima Prefecture with carbon and nitrogen concentrations and stable  
499 isotope ratios. *Science of the Total Environment*

500 Lane SN, Reaney SM, Heathwaite AL. 2009. Representation of landscape hydrological connectivity  
501 using a topographically driven surface flow index: hydrological connectivity. *Water Resources*  
502 *Research* **45(8)**:W08423.

503 Lepage H, Evrard O, Onda Y, Chartin C, Lefèvre I, Ayrault S, Bonté P. 2014b. Tracking the origin  
504 and dispersion of contaminated sediments transported by rivers draining the Fukushima radioactive

505 contaminant plume. Proceedings of a symposium held in New Orleans, Louisiana, USA, (11–14  
506 December 2014), *IAHS Publ.* **367**: 237-245.

507 Lepage H, Evrard O, Onda Y, Patin J, Chartin C, Lefèvre I, Bonté P, Ayrault S. 2014a. Environmental  
508 mobility of  $^{110m}\text{Ag}$ : lessons learnt from Fukushima accident (Japan) and potential use for tracking  
509 the dispersion of contamination within coastal catchments. *Journal of Environmental Radioactivity*  
510 **130**: 44–55.

511 López-Vicente M, Poesen J, Navas A, Gaspar L. 2013. Predicting runoff and sediment connectivity and  
512 soil erosion by water for different land use scenarios in the Spanish Pre-Pyrenees. *Catena* **102**: 62-73.

513 Ministry of Education, Culture, Sports Science and Technology (MEXT). 2011. Preparation of  
514 distribution map of radiation doses, etc. (Map of radioactive cesium concentration in soil) by MEXT.  
515 [http://radioactivity.mext.go.jp/en/contents/5000/4165/24/1750\\_083014.pdf](http://radioactivity.mext.go.jp/en/contents/5000/4165/24/1750_083014.pdf).

516 Motha JA, Wallbrink PJ, Hairsine PB, Grayson RB. 2002. Tracer properties of eroded sediment and  
517 source material. *Hydrological Processes* **16**: 1983–2000.

518 Mouri G, Golosov V, Shiiba M, Hori T. 2014. Assessment of the cesium-137 flux adsorbed to  
519 suspended sediment in a reservoir in the contaminated Fukushima region in Japan. *Environmental*  
520 *Pollution* **187C**: 31–41.

521 Nagao S, Kanamori M, Ochiai S, Tomihara K, Fukushi K, Yamamoto M. 2013. Export of  $^{134}\text{Cs}$  and  
522  $^{137}\text{Cs}$  in the Fukushima river systems at heavy rains by Typhoon Roke in September 2011.  
523 *Biogeosciences* **10**: 6215–6223.

524 Ohmori H. 1991. Change in the mathematical function type describing the longitudinal profile of a  
525 river through an evolutionary process. *Journal of Geology* **99**: 97-110.

526 Oguchi T., 1997. Late Quaternary sediment budget in alluvial-fan-source-basin systems in Japan.  
527 *Journal of Quaternary Science* **12**: 381-390.

528 Parsons AJ, Brazier RE, Wainwright J, Powell DM. 2006. Scale relationships in hillslope runoff and  
529 erosion. *Earth Surface Processes and Landforms* **31**: 1384–1393.

530 Renard KG, Foster GR, Weesies GA, McCool D, Yoder D. 1997. Predicting soil erosion by water: a  
531 guide to conservation planning with the revised universal soil loss equation (RUSLE). USDA (eds).  
532 Agriculture Handbook: Washington, 703.

533 Renard KG, Foster GR, Weesies GA, Porter JP. 1991. RUSLE: Revised universal soil loss equation.  
534 *Journal of soil and Water Conservation* **46(1)**: 30-33.

535 Saito K, Tanihata I, Fujiwara M, Saito T, Shimoura S, Otsuka T, Onda Y, Hoshi M, Ikeuchi Y,  
536 Takahashi F. 2015. Detailed deposition density maps constructed by large-scale soil sampling for  
537 gamma-ray emitting radioactive nuclides from the Fukushima Dai-ichi Nuclear Power Plant accident.  
538 *Journal of environmental radioactivity* **139**: 308-319.

539 Shiono T, Kamimura K, Okushima S, Fukumoto M. 2002. Soil loss estimation on a local scale for soil  
540 conservation planning. *Japan Agriculture Research Quaterly* **36(3)**: 157-161.

541 Tamura T. 1964. Consequences of activity release: selective sorption reactions of cesium with soil  
542 minerals. *Nuclear Safety* **5**: 262–268.

543 Thornton B, Ohnishi, S, Ura T, Odano N, Sasaki S, Fujita T, Watanabe T, Nakata K, Ono T, Ambe D.  
544 Distribution of local <sup>137</sup>Cs anomalies on the seafloor near the Fukushima Daiichi Nuclear Power  
545 Plant, *Mar. Pollut. Bull.* **74**: 344–350.

546 Ueda S, Hasegawa H, Kakiuchi H, Akata N, Ohtsuka Y, Hisamatsu S. 2013. Fluvial discharges of  
547 radiocesium from watersheds contaminated by the Fukushima Dai-ichi Nuclear Power Plant accident,  
548 Japan. *Journal of Environmental Radioactivity* **118**: 96–104.

549 USDA. 2013. Rainfall Intensity Summarization Tool (RIST), United States Department of Agriculture  
550 (USDA), Agriculture Research Service, National Sedimentation Laboratory, Oxford, Mississippi,  
551 Version 3.88.

552 Wainwright J, Parsons AJ, Powell DM, Brazier RE. 2001. A new conceptual framework for  
553 understanding and predicting erosion by water from hillslopes and catchments. In Ascough JC,  
554 Flanagan DC (eds). Soil Erosion Research for the 21st Century. Proceedings of the International  
555 Symposium, Thomas DSG (ed). American Society of Agricultural Engineers: St Joseph, MI; 607–610.

556 Wischmeier WH and Smith DD. 1978. Predicting rainfall erosion losses-A guide to conservation  
557 planning. Predicting rainfall erosion losses-A guide to conservation planning. USDA (eds.).  
558 Agriculture Handbook: Washington, 537.

559 Wood, S. N. 2001. mgcv: GAMs and generalized ridge regression for r. *R news* **1(2)**: 2-25.

560 Yamaguchi M., Kitamura A., Oda Y., Onishi Y. 2014. Predicting the long-term <sup>137</sup>Cs distribution in  
561 Fukushima after the Fukushima Dai-ichi nuclear power plant accident: a parameter sensitivity  
562 analysis. *Journal of Environmental Radioactivity* **135**: 135–146

563 Yamashiki Y, Onda Y, Smith HG, Blake WH, Wakahara T, Igarashi Y, Matsuura Y, Yoshimura K.  
564 2014. Initial flux of sediment-associated radiocesium to the ocean from the largest river impacted by  
565 Fukushima Daiichi Nuclear Power Plant. *Scientific Reports* **4**, 3714.

566 Yoshikawa S, Yamamoto H, Hanano Y, Ishihara A. 2004. Hilly-land Soil Loss Equation (HSLE) for  
567 evaluation of soil erosion caused by the abandonment of agricultural practices. *Japan Agricultural*  
568 *Research Quarterly* **38(1)**: 21-29.

569

570 Table 1. Observed and predicted rainfall erosivity mean and standard deviation (SD) ( $EI_{30}$  in  $MJ\ mm\ ha^{-1}\ h^{-1}$ ) for major events that occurred during each  
 571 typhoon season since the nuclear accident within the 100 km area around the FDNPP, and parameters describing performance of the GAMs used to map  $EI_{30}$   
 572 in the area.

Typhoon event	Date	Number of stations	Observed $EI_{30}$		Predicted $EI_{30}$		Model performance		
			Mean	SD	Mean	SD	ME	RMSE	$R^2$
Roke	Sept. 8-22, 2011	39	1695	1066	1706	1005	11.6	289.0	0.89
Jelawat	Sept. 20 - Oct. 1, 2012	36	262	197	269	168	7.4	80.3	0.83
Wipha & Francisco	Oct. 9-26, 2013	39	549	317	551	298	2.1	80.8	0.89
Phanfone & Vongfong	Sept. 28 - Oct. 14, 2014	40	1034	759	1033	721	3.5	159.6	0.95
Etau	Sept. 6 - 9, 2015	40	1581	1577	1554	1489	-26.4	588.0	0.86

573

574 Table 2. Mean rainfall erosivity ( $EI_{30}$  in  $MJ\ mm\ ha^{-1}\ h^{-1}$ ) and standard deviation (SD) of major  
575 events that occurred during each typhoon season since the FDNPP accident for Mano and Niida  
576 catchments (statistics were computed by zonal statistics tool in ArcGis 10.3 and based on  $EI_{30}$  maps  
577 presented in Figure 6B).

Typhoon event	Date	Mano catchment		Niida catchment	
		Mean $EI_{30}$	SD	Mean $EI_{30}$	SD
Roke	Sept. 8-22, 2011	2099	520	1826	646
Jelawat	Sept. 20 - Oct. 1, 2012	187	62	209	67
Wipha & Francisco	Oct. 9-26, 2013	653	146	608	209
Phanfone & Vongfong	Sept. 28 - Oct. 14, 2014	1469	941	1231	941
Etau	Sept. 6 - 9, 2015	4299	1702	4124	1602

578

579

580

581 Table 3. Mean revised Connectivity Index ( $IC_{rev}$ ) and standard deviation (SD) of major events  
 582 occurred during each typhoon season since the FDNPP accident for the Mano and Niida catchments  
 583 (Statistics were computed by zonal statistics tool in ArcGis 10.3 and based on  $IC_{rev}$  maps presented in  
 584 Figure 7).

Typhoon event	Date	Mano catchment		Niida catchment	
		Mean $iC_{rev}$	SD	Mean $I_{crev}$	SD
Roke	Sept. 8-22, 2011	-7.6	1.3	-7.8	1.4
Jelawat	Sept. 20 - Oct. 1, 2012	-9.8	1.5	-9.8	1.4
Wipha & Francisco	Oct. 9-26, 2013	-8.7	1.4	-8.8	1.4
Phanfone & Vongfong	Sept. 28 - Oct. 14, 2014	-8.2	1.4	-8.4	1.4
Etau	Sept. 6 - 9, 2015	-7.2	1.5	-7.2	1.4

585

586

587

588

589

590

591

592

593

594

595

596

597

598

599

600 **Figure captions**

601 Figure 1. Spatial variability of the radiocaesium contamination plume in the eastern part of Fukushima  
602 Prefecture with locations of the 40 meteorological stations within a 100 km buffer around the FDNPP  
603 (dashed line) and the two investigated catchments (full black line).  $^{137}\text{Cs}$  activities are decay corrected  
604 to March 11 2011 (Chartin et al., 2013)

605 Figure 2. Mean daily rainfall from the 40 meteorological stations located in the 100 km buffer around  
606 the FDNPP (Fig.1) from March 2011 to November 2015 (FW indicates field work sampling  
607 campaigns; tropical storms and typhoons are highlighted by the dashed arrows).

608 Figure 3. Elevation (A) and dominant land cover classes (B) for the Mano and Niida catchment.

609 Figure 4. Box-plots of  $^{137}\text{Cs}$  contamination (in  $\text{kBq kg}^{-1}$ ) in sediment sampled in Mano and Niida  
610 rivers after each typhoon season since the FDNPP accident  $^{137}\text{Cs}$  activities are decay corrected to 11  
611 March 2011; outliers were excluded from the datasets and the red dots in the box plots indicate the  
612 mean concentrations.

613 Figure 5. Sediment enrichment ratio (ER) values measured after each typhoon season since the  
614 FDNPP accident.

615 Figure 6. Rainfall erosivity ( $\text{EI}_{30}$  in  $\text{MJ mm ha}^{-1} \text{h}^{-1}$ ) of the most intensive typhoons that occurred prior  
616 each sampling campaigns since the FDNPP accident for the catchments containing the main  
617 radioactive contamination plume (A) and for the two investigated catchments (B).

618 Figure 7. The revised connectivity index (ICrev) for the typhoons that occurred prior each sampling  
619 campaign since the FDNPP accident.

620 Figure 8. Relationships between the revised Index of Connectivity (ICrev) and the Enrichment Ratio  
621 values (ER\*) for sediment sampled the Mano river (grey) and the Niida river (black).

622

623

624

625

626

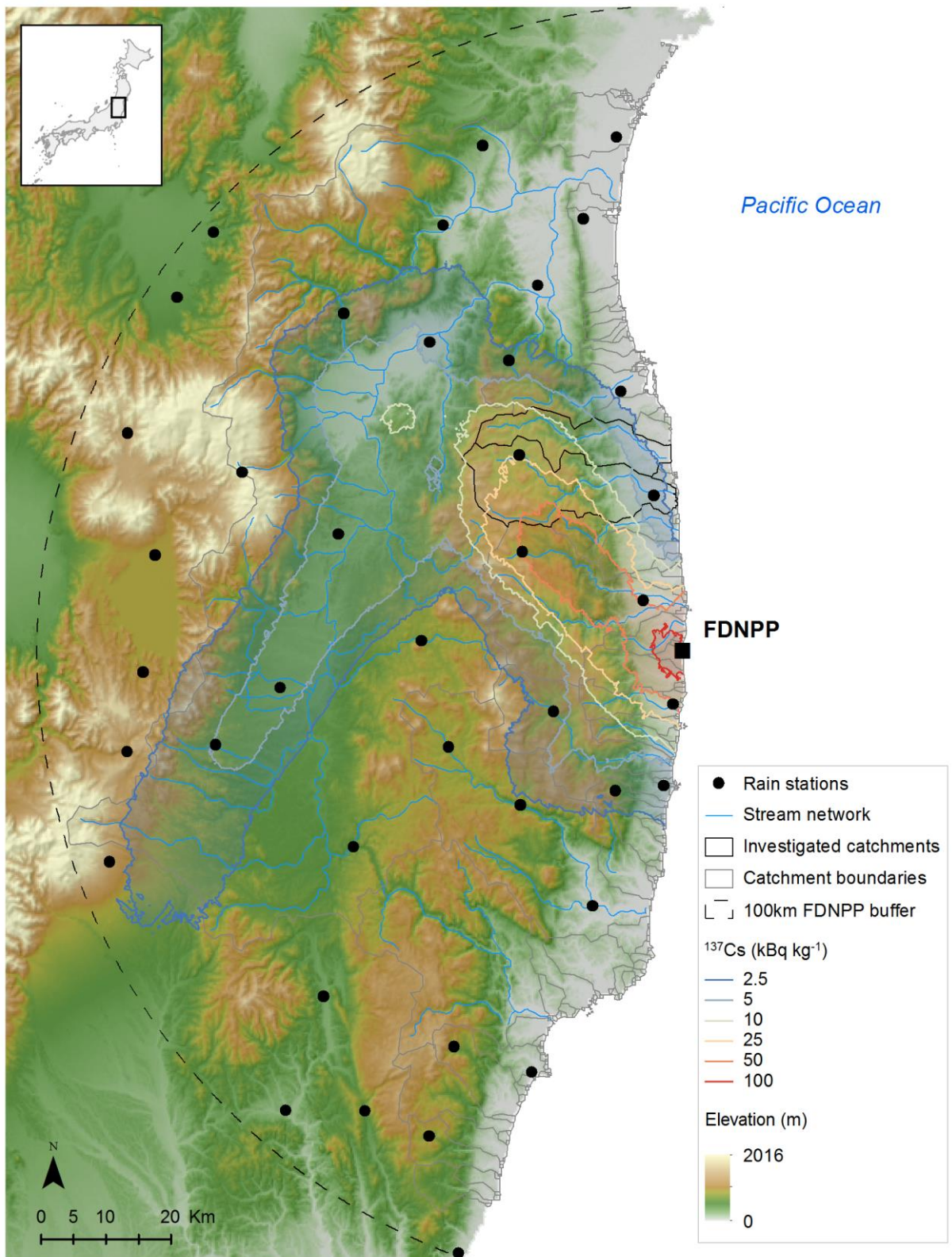
627

628

629

630

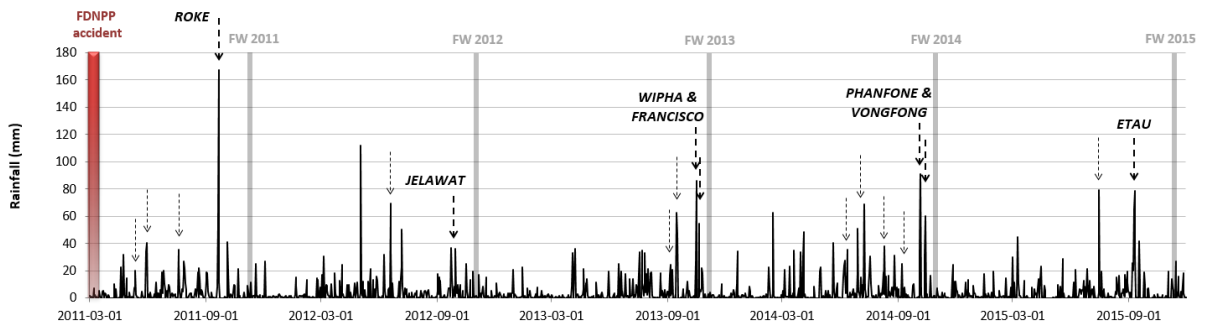
631 Figure 1.



632

633

634 Figure 2.



635

636

637

638

639

640

641

642

643

644

645

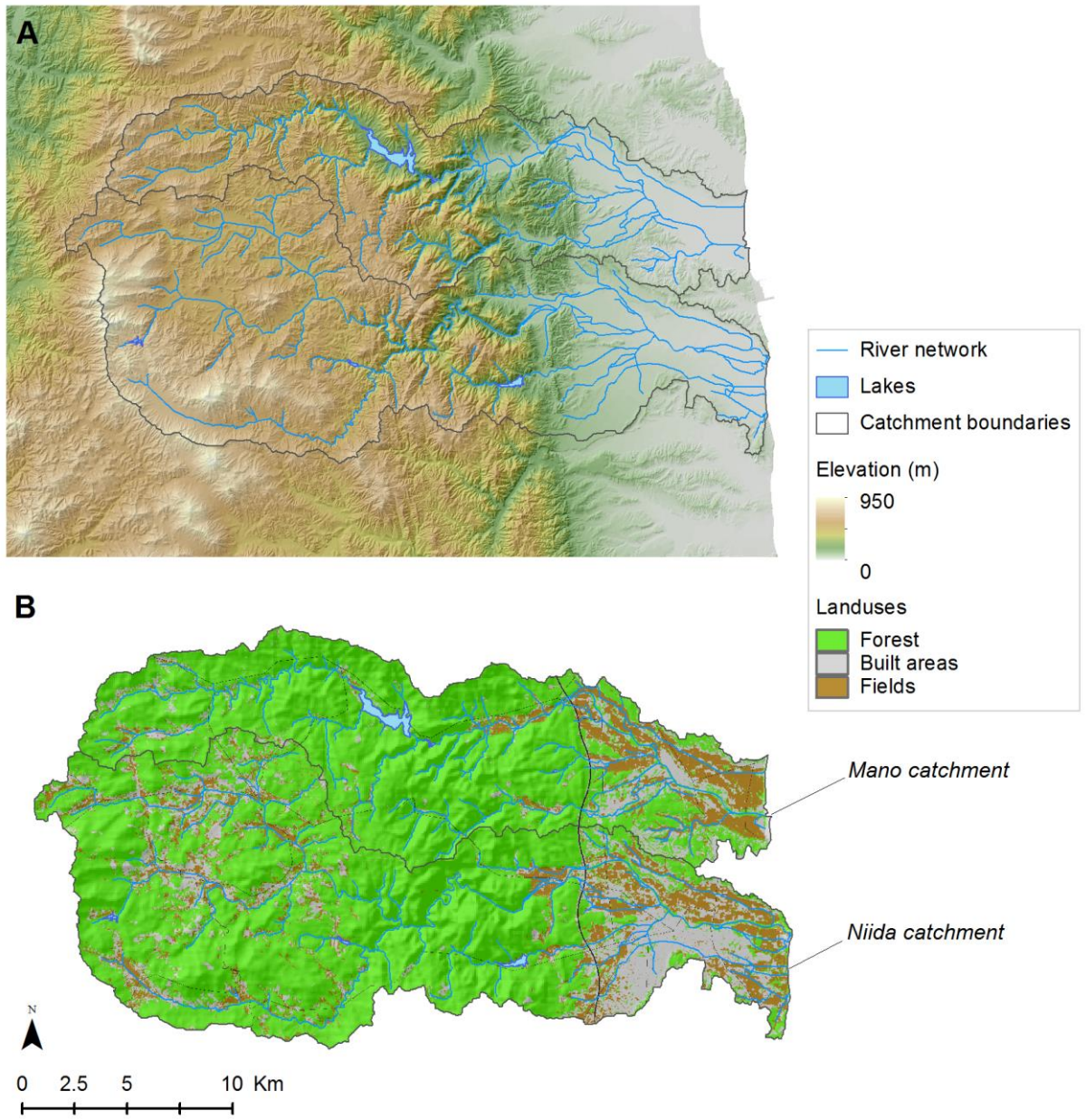
646

647

648

649

650



652

653

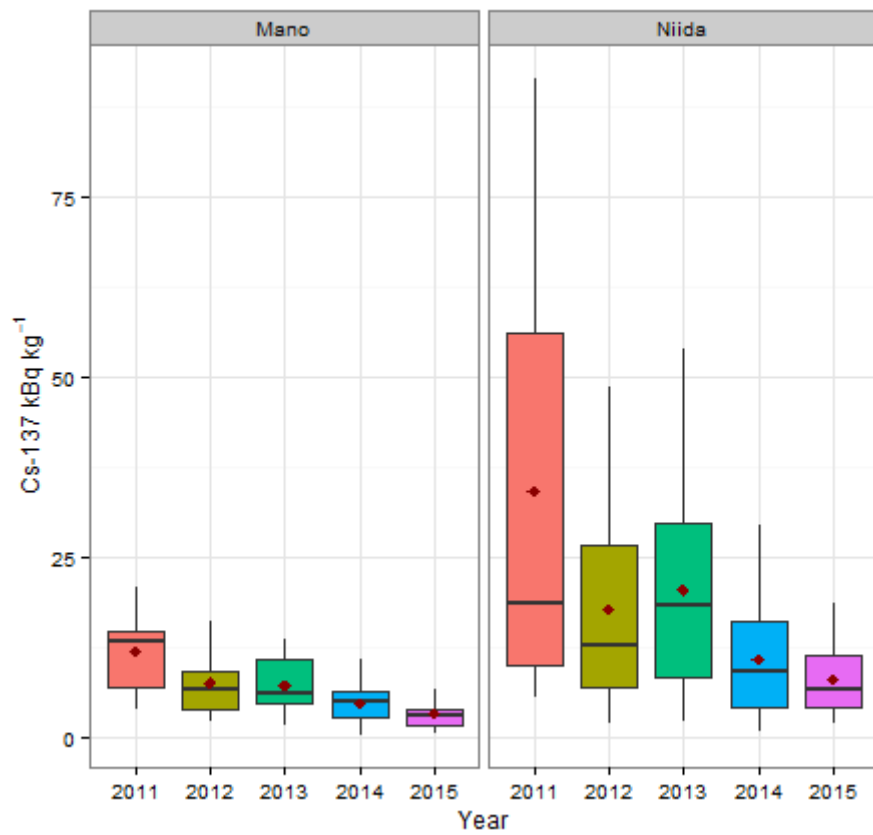
654

655

656

657

658 Figure 4.



659

660

661

662

663

664

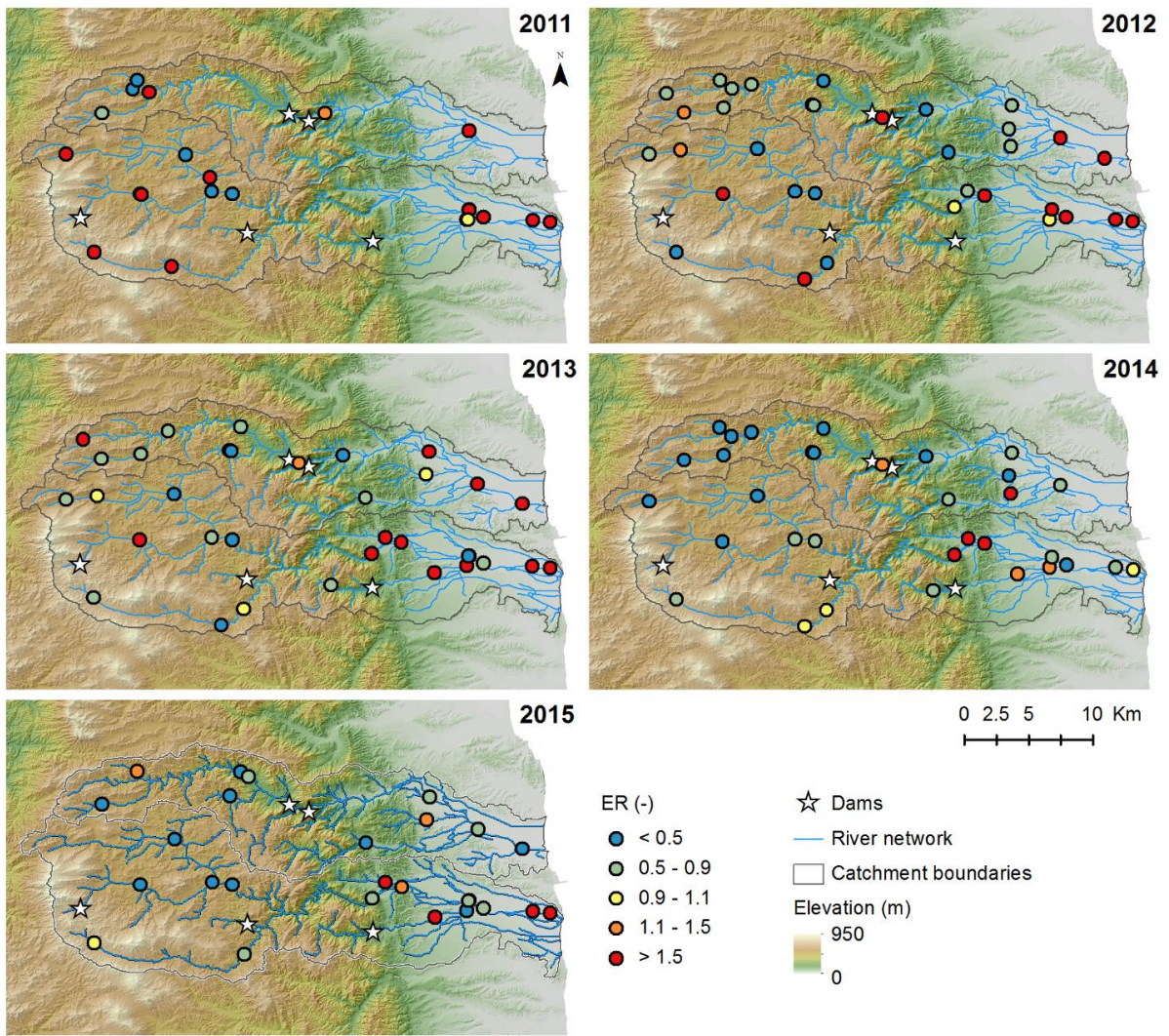
665

666

667

668

669 Figure 5.



670

671

672

673

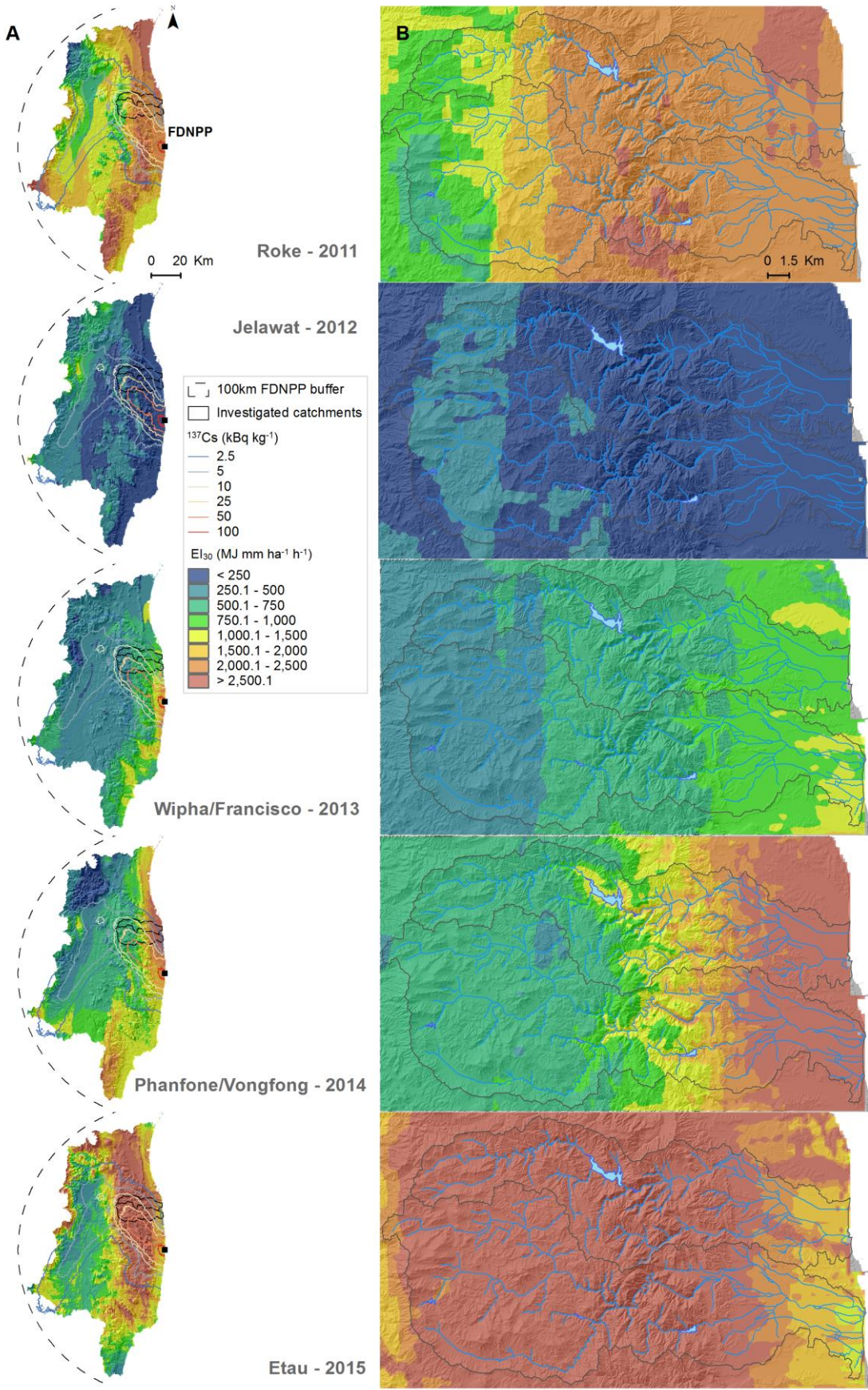
674

675

676

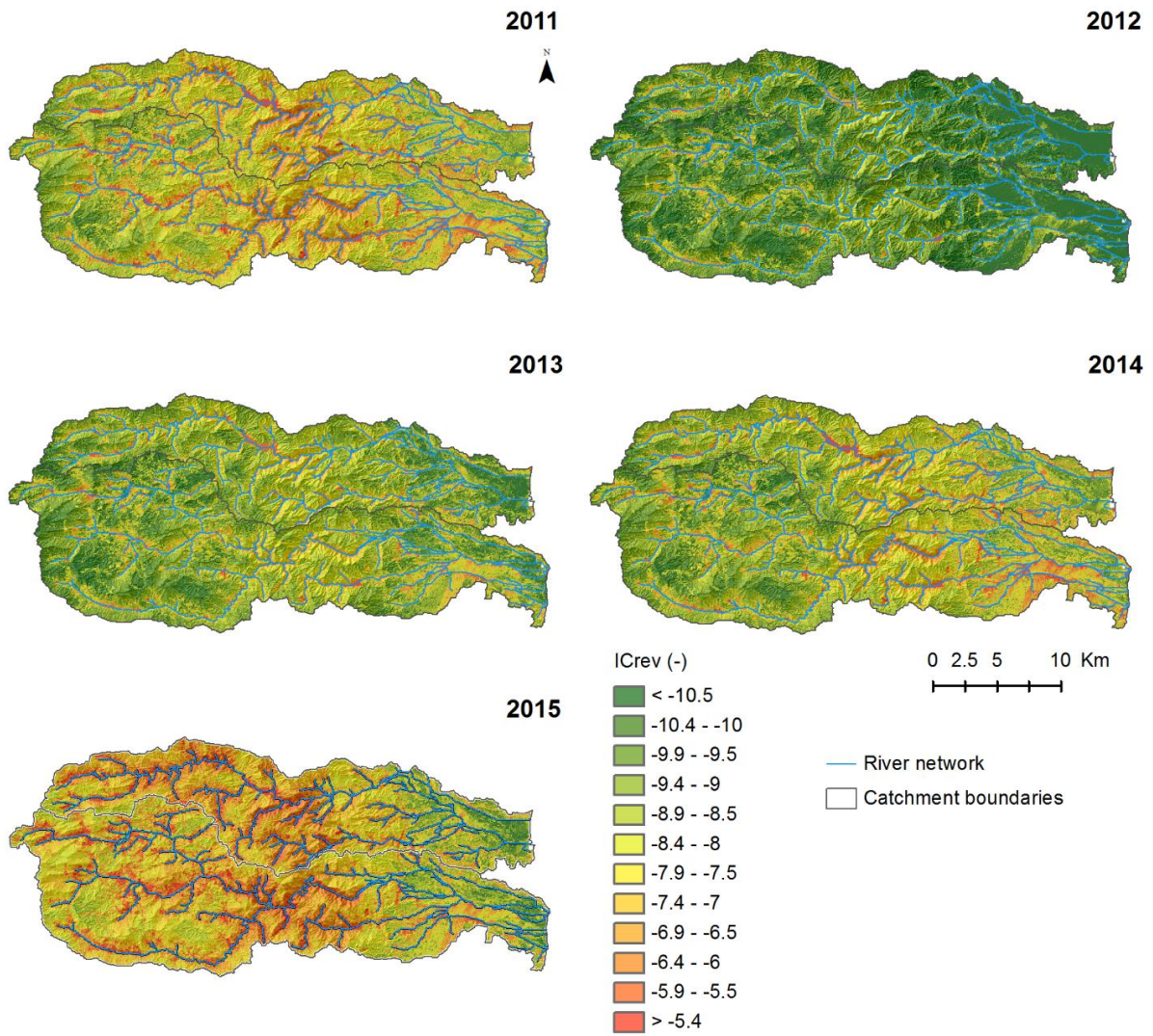
677

678 Figure 6.



679

680 Figure 7.



681

682

683

684

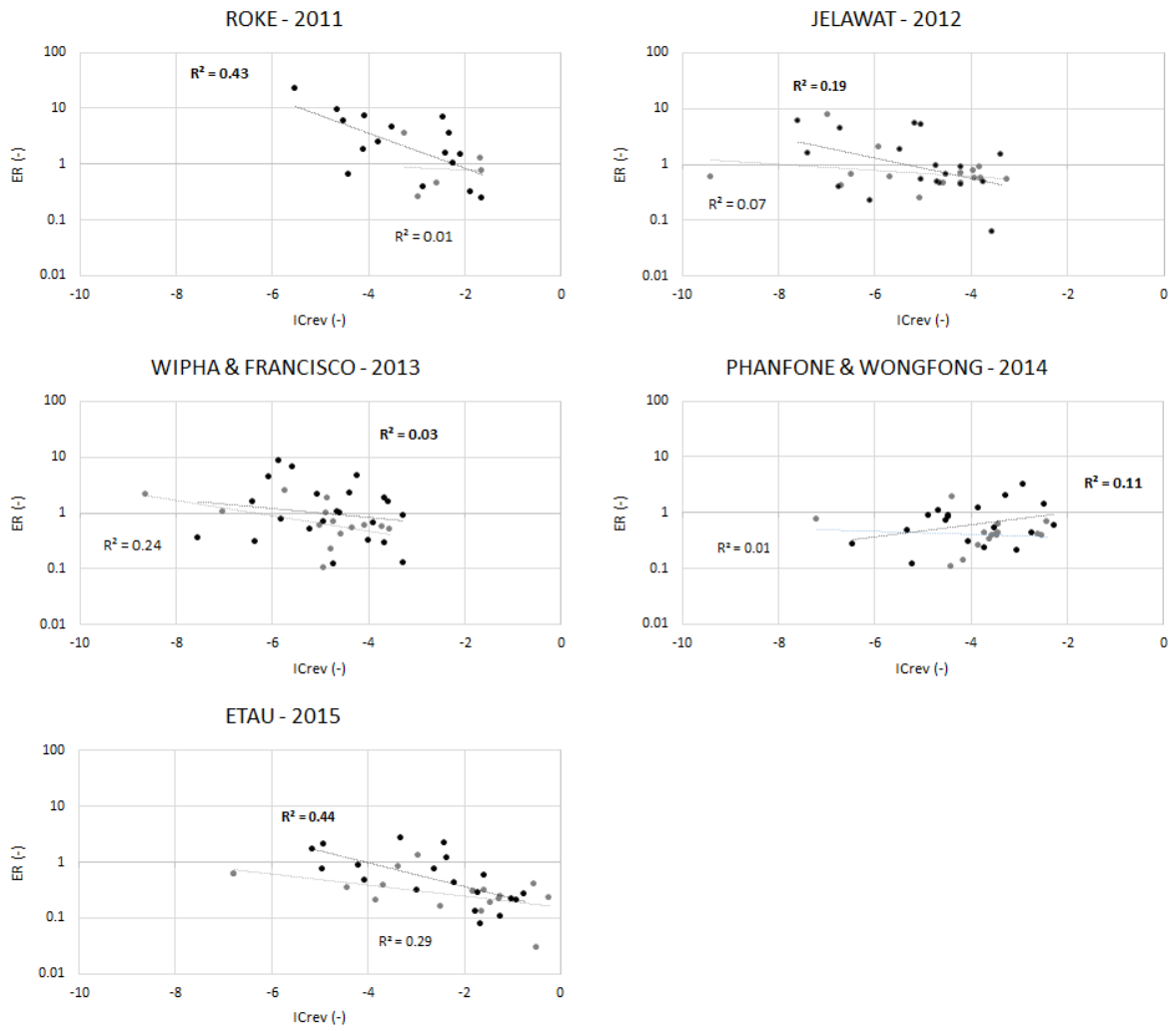
685

686

687

688

689 Figure 8.



690